An experimental investigation of forced steady rotating turbulence

Gan L.[a,*], Baqui Y. B.[b], Maffioli A.[c]

[a]*School of Engineering and Computing Sciences, Durham University, DH1 3LE, UK*
[b]*Department of Engineering, University of Cambridge, CB2 1PZ, UK*
[c]*KTH Mechanics, Osquars Backe 18, Stockholm 10044, Sweden*

Abstract

This paper presents some of the principal findings of an experimental investigation of forced statistically steady turbulence in a rapidly rotating background. The experiment is conducted in a large cylindrical mixing tank and bulk rotation is produced by two large co-rotating impellers installed near the top and the bottom of the tank. The mean flow motion generated in such a configuration is axisymmetric and close to but not exactly solid-body rotation. The focus of this work is on the region in the vicinity of the rotation axis where the flow is Rayleigh stable. The unique features of this facility allows forcing and thus permits turbulence to be maintained at a certain level without a mean decay. The facility also allows an easy experimental access of statistical quantities. The bulk rotation rates and the amount of turbulence are adjusted to a Rossby number (Ro) of $O(1)$. Under this condition, some physical phenomena commonly seen in solid-body rotating turbulent flows at low Ro are also observed, despite the differences in other parameters. A flow visualization at one of the testing conditions using pearlescence clearly shows the presence of cyclonic columnar structures. Two-dimensional particle image velocimetry (2DPIV) measurements are carried out in a plane normal to the axis of the rotation and near the middle height of the tank. Symmetry breaking between cyclonic and anti-cyclonic vorticity in the flow is revealed by the skewness of

*Email: lian.gan@durham.ac.uk

the fluctuating vorticity. It is found that skewness is not a monotonic function of Ro; in this particular experimental arrangement, symmetry is broken to a maximum extent at Ro$\sim$ 1.5 based on velocity length scale. Turbulence quantities are also computed along with the turbulent energy dissipation, which is estimated using velocity structure functions and lends support to previous findings that purport that dissipation is suppressed in such flows.

Keywords: non-solid-body rotating turbulence, forced steady, experiments

1. Introduction

Turbulence under strong solid-body rotation is one of the canonical turbulent flows which has been the subject of many intense studies. This is primarily due to a well-known striking phenomenon: under certain conditions, long columnar eddies spontaneously form and align with the rotation axis. Nearly all of these studies investigate a turbulent fluid on a rotating platform undergoing solid-body rotation. Detailed analysis of the experimental observations showed that, among the columnar eddies, the cyclonic ones, which spin in the same direction as the bulk rotation, dominate the oppositely spinning anti-cyclones[7]. The presence of these columnar eddies were also found to reduce the turbulence dissipation rate compared to an equivalent non-rotating case. However, very few studies, if any, address the case where the rotation is not of a solid-body type.

In theoretical analysis, which is conventionally conducted for the solid body rotation case, the rotating turbulence problem is often presented in a frame of reference which rotates together with the bulk fluid motion. In such a rotating reference frame, the Navier-Stokes equation for the fluctuating velocity $\mathbf{u}'$ can be written as:

$$\frac{\partial \mathbf{u}'}{\partial t} + (\mathbf{u}' \cdot \nabla)\,\mathbf{u}' = -\nabla\left(\frac{p}{\rho}\right) + 2\mathbf{u}' \times \mathbf{\Omega} + \nu\nabla^2\mathbf{u}', \tag{1}$$

in which p is the reduced-pressure which incorporates the irrotational centrifugal force. Since the rotation of the reference frame occurs along a single direction,

$\mathbf{\Omega}$ can be replaced by $\Omega_{\|}$. The use of the non-inertial rotational reference frame gives rise to the Coriolis term in the conventional Navier-Stokes equation; see the second term on the *r.h.s.* of (1).

Such flow problems are then typically characterised by the Rossby number $\mathrm{Ro} = u'/(\Omega l)$, where u' represents a characteristic fluctuating velocity scale and l represents a suitably defined length scale, conventionally the integral scale of the flow. Ro is essentially a measure of the ratio of inertial to Coriolis forces. The value of Ro is of particular importance because nearly all the column formation observed in experiments occur when Ro is small and the Reynolds number Re (defined as $u'l/\nu$, $\nu =$ kinematic viscosity) is not too low. Under such conditions, the symmetry between the stabilisation characteristics of eddies with cyclonic and anti-cyclonic vorticity starts to break apart[9, 19], resulting in the cyclonic dominance mentioned earlier. Mathematically, this condition of small Ro and high Re, permits the reduction of (1) to a wave-like equation where the Coriolis term gives rise to inertial waves - the linear propagation of which is crucial in explaining the formation of columnar structures[3, 2, 10]. This theory is supported by findings in physical [17, for example] and numerical [16, among others] experiments. The other proposed explanation of the formation of these structures is via the mechanisms of non-linear wave interaction theory [20], the conclusions of which are also consistent with some numerical findings [21], e.g. the trend of increasing anisotropy. The real physics of the formation of these organised structures is very likely a complex combination of the two mechanisms. A further discussion on the formation theories can be found in Ref. 3 Chapter 8.

Most experimental studies on solid-body rotating turbulence thus far have also mainly focused on the decaying behaviour of the flow, aiming to explain the formation and evolution of the columnar structures or the effect these have on the turbulence decay rate. In these experiments, approximately homogeneous turbulence was generated by towing a grid through the container[11, 17]. Once the motion of the grid was stopped, both Re and Ro were allowed to decrease with the progressing free decay of the turbulence. (An exception to this type of

experiment is the pioneering study of Hopfinger et al.[7], in which a fixed oscillating grid frequency was applied to force the turbulence to a quasi-steady state. The results of that work, however, were mainly based on visualisations.) These decaying experiments had two advantages: firstly, the turbulence can be introduced in a relatively homogeneous manner; secondly, the temporal evolution of various quantities can be investigated, e.g. the formation process, which among other findings, were crucial in showing that decay of turbulence is prolonged in a rapidly rotating environment due to the presence of organised columnar eddies. However, these experimental configurations have some important limitations: they do not permit the spatial statistics of the flow to be easily studied as spatial quantities vary with the temporal evolution of the flow; nor do they allow one to understand the dynamical evolution of columnar structures independent of the overall decaying turbulence - a feat that would only be achievable if the flow were statistically steady.

Finally, despite some advantages of using solid-body rotation discussed earlier, the flow resulting from such a form of rotation represents an idealised version of rotating turbulence that does not adequately depict the type of flows encountered in nature e.g. hurricanes, or in applications such as cyclonic separators, pumps and turbines. In most real world systems, turbulence production and rotation occur simultaneously, not in isolation. Such systems, unlike most of the previous experiments, do not decay with time and are often likely to reach a steady state condition and moreover, their motions most likely cannot be described as solid-body rotation. As long as the flow is Rayleigh stable though (which is true for solid-body rotation), inertial waves are still able to play a part in shaping the turbulence and give rise to column formation, implying that concepts developed in the idealised solid-body rotating turbulence experiments are by no means useless in explaining real-world observations. Nevertheless, a comprehensive understanding of commonly encountered rotating turbulence necessitates a large-scale experimental study of non-decaying non-solid-body rotating turbulence which is the goal of the work presented here.

In this study, we generate statistically steady rotating turbulence by means

of co-rotating impellers in a large mixing tank apparatus which is introduced in detail in § 2. To the best of the authors' knowledge, the apparatus represents the largest of its kind utilized to investigate rotating turbulence. In the impeller driven flow produced by this apparatus, boundary effects cannot obviously be explicitly avoided but because the apparatus is very large and the rate of rotation is modest, in regions close to the center of the tank, the flow motion is relatively free from such effects and is similar to but not exactly solid-body rotation. We will show that in the central region, the flow motion is also Rayleigh stable. Unlike the solid-body rotation experiments though, turbulence generated at the boundary and the impeller uniformly seep into this central region, producing the desired result of flow motion without a mean decay. The level of turbulence generation can be further controlled by means of symmetrically placed baffles on the tank walls, see § 2. Because of the large scale of the apparatus, columnar eddies, if they exist, should be able to grow vertically for a much longer time than conventional experiments before being significantly affected by boundary or surface problems.

The experimental apparatus used also enables investigations of the statistics of the flow properties such as turbulence quantities, as well as the structural properties of organised eddies e.g. size and lifetime of cyclonic and anti-cyclonic eddies in the flow. In this paper we aim to focus on the first of these issues: the statistics of the turbulent flow properties.

2. Experimental methodology

It has been mentioned that the experimental apparatus of most, if not all, the previous studies have potential confinement effects due to the limitation of their physical sizes relative to the coherent eddy sizes, especially along the direction of the rotation axis. The spatial constraint in this direction may cause an image effect due to the boundary which influences the eddy structures. In order to address this issue, the experiment is conducted in a large mixing tank which, to the best of the authors' knowledge, is currently the largest facility of

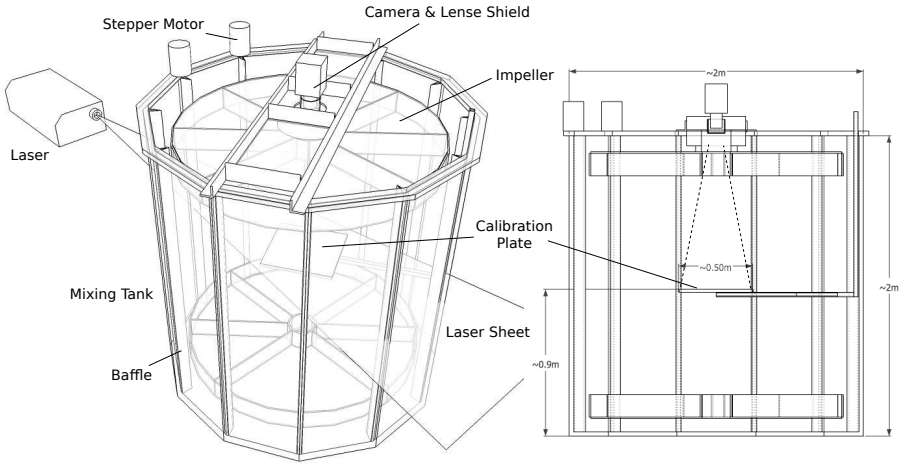

Figure 1: Schematic diagram of the experimental arrangement and the central cross section of the mixing tank. The camera is purposely lifted up from the real position in order to show the lens shield which is used to eliminate the surface effect. The dashed lines (−−) represent the camera lines-of-sight. The diagram is not to scale.

this type. A sketch of this facility is presented in Figure 1.

The tank is a dodecagonal shaped container built on a concrete floor with the top-end open. It has a radius $R_t \approx 1000$ mm, height 2000 mm and is made of 15 mm thick perspex, and is thus transparent from all viewing angles above the floor. Two impellers made of ≈ 5 mm perspex sheet with $\varnothing \approx 1600$ mm are mounted ≈ 100 mm inward from the top and the bottom surfaces of the tank. Each impeller has eight blades that are about 150 mm wide and 5 mm thick, and is independently driven by a stepper motor through a belt system which is able to rotate at a maximum rate of 4.67 rpm when the tank is filled up. When the two impellers rotate at the same rate and in the same direction, a bulk rotational environment can be generated at the centre of the tank, some distance away from the tank wall. It is worth stressing that although the rotation produced in the tank central region by this mechanism is axisymmetric, it is not exactly solid-body rotation. This fact will be confirmed in § 3.2. In this study, four different impeller rotation rates are employed; see table 1.

Freq. (kHz)	6	4	2	1
Ω (rpm)	4.000	2.667	1.333	0.667
Ω (rad/s)	0.418	0.279	0.140	0.070

Table 1: The four impeller rotation rates employed in this study and the speed conversions. Abbreviations: Freq.: stepper motor frequency; rpm: impeller rotation rate in *round/minute*.

An important feature of this rig is the 12 Λ-shaped baffles installed along each corner of the tank wall, as is shown in Figure 1. The baffles are made of aluminium sheet with a height of $\approx$ 100 mm extended into the fluid and they can be detached. The function of these baffles in this experiment is to help shed oppositely sensed vortices and hence inject turbulence into the bulk rotation. It is apparent that due to the location of the baffles, the turbulence intensity distribution inside the tank is not homogeneous but is a function of radial distances. Nevertheless these baffles offer a unique advantage in the sense that, if the rotation rate of the impellers is steady, the turbulence generation rate from these baffles can also be maintained at a steady level. The resultant turbulence in the bulk rotating fluid in this case will be in a forced steady state. On average, the amount of turbulence in the tank can be controlled by the number of baffles, although we will see later that this effect is not linear. In this experiment, three baffle number conditions are adopted as a way of controlling the turbulence level: B12 (12 baffles), B6 and B3. For B6, every other baffle is removed and for B3, every third is kept and others removed. The baffles are removed or retained in this manner to ensure that the turbulence energy distribution inside the tank remains as axisymmetric as possible.

A simple 2DPIV system is used to extract the two-dimensional two-component (2D2C) velocity information over a horizontal plane in the central area of the tank. The PIV sampling rate is set according to different impeller rotation rates such that 45 samples are gathered for one complete impeller revolution. In this way, the relative temporal resolution for all the cases is fixed. At this recording rate, one camera buffer allows 2728 velocity fields to be recorded which

corresponds to 60.6 impeller revolutions.

In an ideal experiment the entire horizontal cross section of the tank would be measured, but in practice this is not possible because the position of the top impeller interferes with the camera's view. The one achieved in this work, which is about 450 mm $\times$ 450 mm, is the largest FOV that could be realised practically. This relatively small FOV however ensures that it is about $3/4R_t$ away from the boundary, thus the boundary effect has very little influence on the measurement domain. More importantly, it ensures that the flow field within the FOV is Rayleigh stable.

The images are cross correlated by 32×32 pix^2 and 75% overlap for the final pass, which gives a spatial resolution of 14 mm based on the interrogation window size and 3.5mm based on vector spacing. When central differencing scheme is applied to calculate spatial derivatives and hence vorticity, every other point (i.e. $i-2$ and $i+2$) is used so that the groups of particles accessed have no overlap. Finally the camera is calibrated by a third-ordered polynomial fit in both directions to account for some minor distortion effects and the particle images are processed to vector fields by DaVis 7.2.

3. Results and discussions

In this section, the results obtained from the mean velocity, the fluctuating velocity and vorticity are presented, followed by the results for the turbulence stresses, the production and an estimation of the dissipation.

3.1. Flow visualisation

In order to confirm the existence of the columnar eddies, pearlescence particles are used to seed the flow and to reflect possible large structures[17]. Pearlescence consists of individual plate-like particles which respond to simple strain and shear [8, 15]. They are useful in flow visualizations as they tend to highlight regions of intense and persistent strains while being insensitive to small scale structures, rendering them ideal for marking large organised structures in a qualitative way.

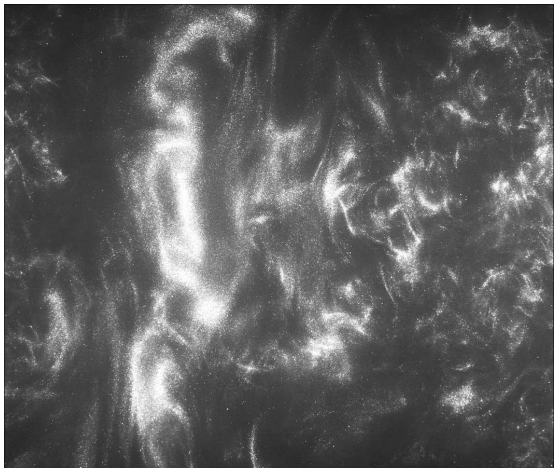

Figure 2: Flow visualisation in a vertical plane in the central region of the tank, using pearlescent particles. The image size is 345×410 mm. The flow condition is at B3/0.14rad/s.

Figure 2 shows an example of the visualisation of a columnar eddy at the flow condition of B3/0.14rad/s. The image shown is from a short video in which this structure is seen to spin cyclonically by itself. The video is recorded by the camera operating at 10Hz recording rate and is focused on a vertical plane in the central area of the tank. The FOV of Figure 2 is about 345 mm in height and 410 mm in width. The FOV is illuminated by a light sheet of 10 mm thickness.

An elongated, twisted columnar-like structure is observed in the left part of Figure 2. Its size is about 50mm in diameter and it spans the height of the FOV. Its shape is quite complex - a little like a broken and twisted double helix for the part shown, comparable to the sketches made in Ref. [7].

3.2. The mean rotational velocity

The notations for various quantities adopted in this article are defined as follows. Taking the horizontal u components in the Cartesian system as examples, we use $\langle\rangle$ for the spatial-averaged quantities; $\tilde{u}$ for the instantaneous velocity; U for the time-mean (ensemble mean); u' for the fluctuating velocity, i.e. $u' = \tilde{u} - U$; u for rms u', i.e. $u = \sqrt{(1/N)\sum_{i=1}^{N} u'^2_i}$; and finally $|u|$ for the rms magnitude since we also have the other velocity component available from

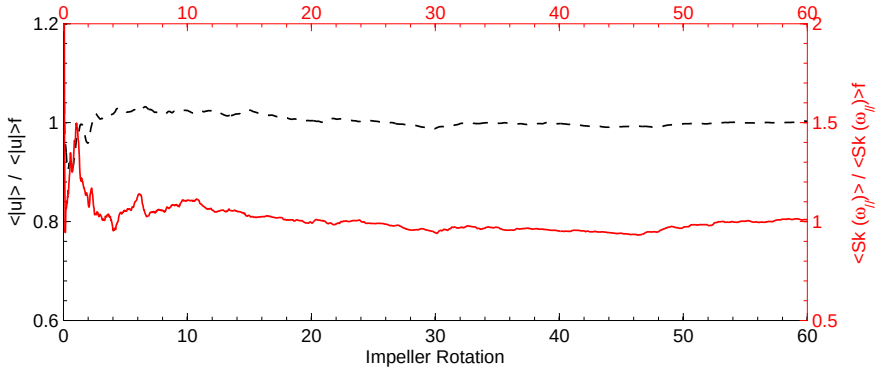

Figure 3: Test for the number of impeller rotations required for satisfactory statistical convergence, for the in-plane spatial mean fluctuating velocity rms magnitude $\langle |u| \rangle$ and the skewness of the fluctuating vorticity $\langle Sk\left(\omega_{\parallel}\right)\rangle$. The right y-axis is for $\langle Sk\left(\omega_{\parallel}\right)\rangle$ $-$, and the left is for $\langle |u| \rangle$ $--$. The two quantities are normalised by their final values, so they both converge to unity.

the measurements.

First, figure 3 shows that 60 impeller rotations are enough to ensure statistical convergence for the two most important turbulence quantities in this study: the in-plane spatially averaged fluctuating velocity rms (root mean square) $\langle |u| \rangle$ and the spatially averaged skewness of fluctuating vorticity $\langle Sk\left(\omega_{\parallel}\right)\rangle$. The convergence of skewness is slower because it is a higher order quantity. The convergence quantity plotted in Figure 3 is calculated according to

$$\langle |u| \rangle_T = \langle \left\{ \frac{1}{T} \int_{t=0}^{T} \left[\tilde{\mathbf{u}}\left(t\right) - \frac{1}{T} \int_{t=0}^{T} \tilde{\mathbf{u}}\left(t\right) \mathrm{d}t \right]^2 \mathrm{d}t \right\}^{1/2} \rangle, \tag{2}$$

and a similar equation for $\langle Sk\left(\omega_{\parallel}\right)\rangle$.

The mean azimuthal velocity U_θ is presented in Figure 4 and we will see that it already displays some unique characteristics of the rotating motion generated in our experiments.

Since the raw 2D2C velocity data are stored in Cartesian coordinates, a simple trigonometric operation is required to map the velocities from Cartesian coordinates to cylindrical coordinates $(\tilde{u}, \tilde{v}) \vdash (\tilde{u}_\theta, \tilde{u}_r)$. After that, they un-

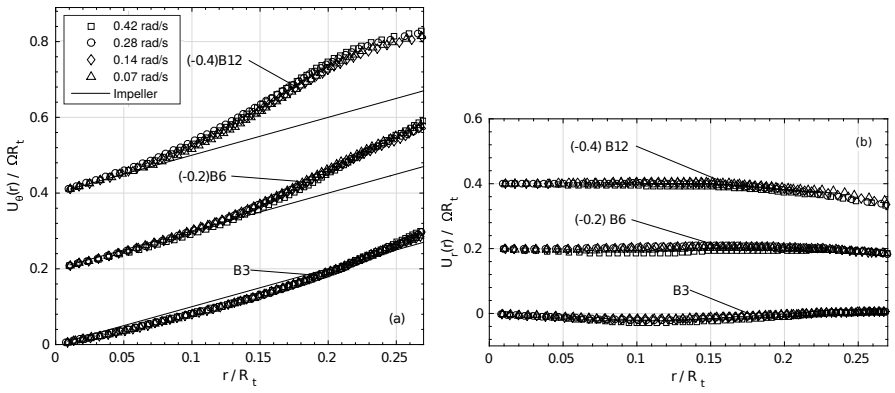

Figure 4: The ensemble averaged mean azimuthal velocity U_θ (a) and the radial velocity U_r (b) as functions of normalised radial position r. B12 and B6 cases are both shifted upwards for the purpose of clearer presentation; their true values can be obtained using the operation marked in the adjacent brackets. This convention applies to all similar plots throughout this paper.

dergo an azimuthal averaging process to give the curves in Figure 4 (a). Two important observations can immediately be made. First, when normalised by ΩR_t, $U_\theta(r)$ is a strong function of baffle number and is self-similar for different Ωs. Later we will see that not only $U_\theta(r)$, but most of the quantities, when plotted against radial distances, show this characteristic as well. The second and more important observation is that the local U_θ at larger r overtakes its driving force - the impeller, quite significantly, especially for the B12 cases. This 'counter-intuitive' observation is most likely the result of the poloidal recirculation induced by the vertical pumping, which intensifies the mean vorticity by a vortex stretching mechanism. The pumping effect is also confirmed by the weak inward radial flow towards larger radii in figure 4(b). It also is not difficult to see from figure 4 (a) that over the entire FOV, the flow is Rayleigh stable, i.e. $\dfrac{\mathrm{d}}{\mathrm{d}r}(rU_\theta) > 0$.

3.3. The fluctuating velocity and vorticity

From now on, the results will be presented in terms of the fluctuating velocity $\mathbf{u}'$ and the fluctuating vorticity $\omega_\parallel$ ($\nabla \times \mathbf{u}'$ projected in the $\parallel$ direction). Note

that $\omega_{\|}$ here is low-pass-filtered with respect to the true vorticity, due to the finite PIV interrogation window size. The scale dependency issue has been discussed previously [6, 13, 5, for example]. When the ensemble mean velocities described in §3.2 are subtracted from the raw instantaneous velocity obtained from the 2DPIV directly, the fluctuating velocities are obtained (see figure 5 for an example), from which the organised large eddies can be clearly visualised in most cases. Figure 6 presents typical quantitative visualisations of such eddies for the most and the least turbulent cases, i.e. B12/0.42rad/s and B3/0.07rad/s respectively. The eddies perhaps are more easily seen in the 2D streamline plots, as the vorticity field is generally more fragmented. Since only 2D velocities are available, these streamlines are computed using the in plane fluctuating velocity only. Two qualitative observations can be immediately made from the streamline plots. First, the nature of the eddies is very irregular and complex in terms of shape; organised eddies can contain both positive and negative small vorticity blobs; second, the eddies are much more intense in B12/0.42rad/s case than those in B3/0.07rad/s, with the size being generally larger than that in the latter.

When all the fluctuating vorticity fields like those plotted in Figure 6 are obtained, the probability density function (PDF) of $\omega_{\|}$ can be examined, which is given in Figure 7. One can see clearly that the shapes of the PDFs of all the three cases are very similar in semi-log plots and that they are not Gaussian. The PDFs of $\omega_{\|}$ are distinguishably asymmetric about zero: the peaks are slightly anti-cyclonic and the tails are clearly more cyclonic, which leads to a non-vanishing skewness. Physically, this suggests that there are more anti-cyclonic weak vorticity and cyclonic strong vorticity in the FOV. The skewness averaged over the FOV for all the cases are listed in table 2 as the global skewness Sk_G, in which the mean *fluctuating* vorticity value $\langle \omega_{\|} \rangle$ over the FOV gives a zero value for all the cases by definition.

The skewness $Sk\left(\omega_{\|}\right)$ puts weight on eddies with larger vorticity magnitude, therefore its spatial mean value Sk_G gives a hint about whether, on average, the dominant intense eddies are cyclonic or anti-cyclonic. The $Sk\left(\omega_{\|}\right)$ shows

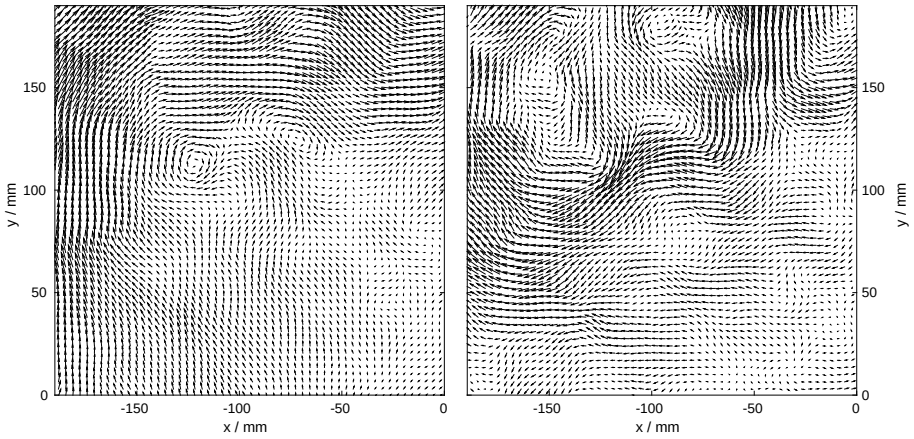

Figure 5: Example of an instantaneous raw vector field (left) and the corresponding fluctuating vector field (after the mean velocity is subtracted) (b). The case shown here is B12/0.42rad/s zoomed in to about a quarter of the FOV.

Ω	Ro_G			Re_G		
rad/s	B12	B6	B3	B12	B6	B3
0.42	3.35	2.38	1.78	5888	4623	2346
0.28	3.13	2.42	1.46	3694	3257	1544
0.14	2.91	2.30	1.38	1835	1679	826
0.07	3.17	2.21	1.44	882	836	354
Ω	$\langle\tilde{\omega_\parallel}\rangle$ 1/s			Sk_G		
rad/s	B12	B6	B3	B12	B6	B3
0.42	4.15	2.95	2.28	0.23	0.35	0.20
0.28	2.42	1.96	1.20	0.29	0.30	0.30
0.14	1.14	0.95	0.59	0.32	0.37	0.31
0.07	0.62	0.48	0.32	0.29	0.37	0.23

Table 2: The Ro_G, Re_G and Sk_G over the entire flow field for all the cases, based on the velocity integral length scale $l_{u\theta}$. These are the spatial mean (global) quantities after ensemble averaging. The spatial mean *raw* vorticity $\langle\tilde{\omega_\parallel}\rangle$ is also listed for reference purpose.

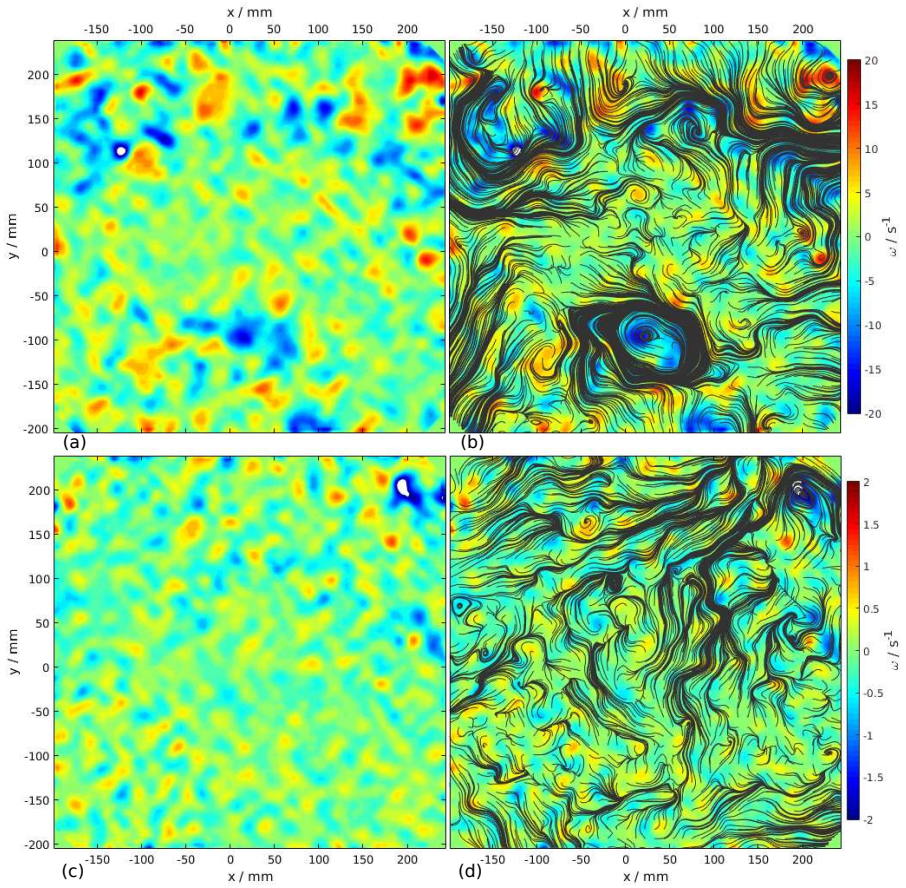

Figure 6: Typical instantaneous visualisations of organised eddies for the most and the least turbulent cases. (a)&(b): B12/0.42rad/s; (c)&(d):B3/0.07rad/s. (a), (c): vorticity contour plots with cyclonic contours marked by blue and anti-cyclonic contours marked by red; contour level:$[\pm 0.1 : \pm 2 : \pm 20.1]$ for (a), $[\pm 00.1 : \pm 0.2 : \pm 2.01]$ for (c). (b)&(d): streamlines with the starting points at every third data point. Typical eddies are located at (x, y) coordinates $(40, -100)$mm in (a) (b), and $(200, 200)$mm in (c) (d).

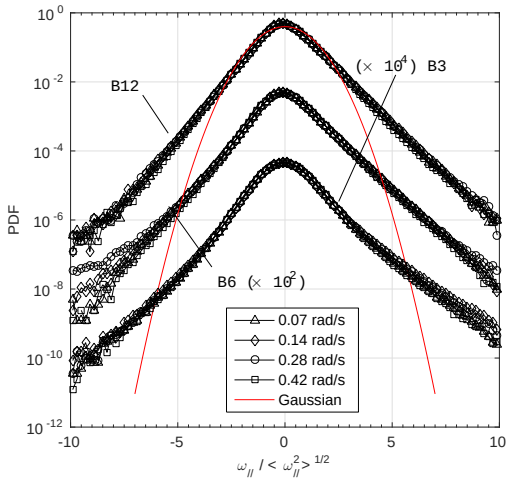

Figure 7: The PDF of the fluctuating vorticity $\omega_{\parallel}$. B6 and B3 cases are shifted downwards.

that cyclonic eddies are prevalent in all the cases which is in agreement with previous works. It needs to be emphasised that Sk_G here includes all the small transient background eddies characteristic of turbulence. It will be shown in § 3.5 that when these background eddies are removed, the cyclonic skewness $Sk\left(\omega_{\parallel}\right)$ becomes more pronounced.

The overall physics observed in the FOV can be inferred from the two governing dimensionless numbers Re and Ro. The length scale involved in defining the two can be estimated by calculating the two-point spatial correlations (TPC) of the fluctuating velocity. Since the nature of the flow generation method indicates that turbulence is homogeneous in the azimuthal direction (θ direction), it is in this direction which TPC is performed, i.e. for the longitudinal component:

$$\mathcal{R}_{u\theta}\left(\theta\right) = \frac{\left\langle u'_{\theta}\left(\mathrm{r},\theta_0\right) u'_{\theta}\left(\mathrm{r},\theta_0+\theta\right)\right\rangle}{\left\langle u'^{2}_{\theta}\left(\mathrm{r},\theta_0\right)\right\rangle}, \tag{3}$$

and likewise for the lateral correlation $\mathcal{R}_{ur}\left(\theta\right)$. Since the turbulence is inhomogeneous in the radial direction, the TPC decorrelation distance depends on the location of the starting point. Figure 8 (a) gives an example of different TPCs as radial locations of the starting point r_o change, from which we may calculate

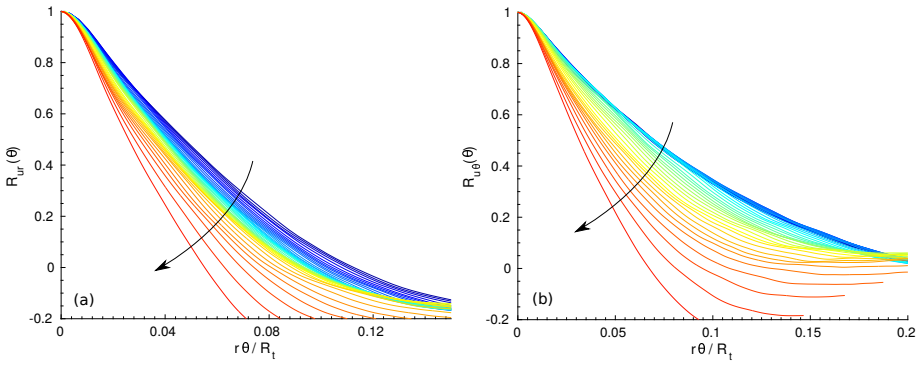

Figure 8: Two-point correlation functions of the fluctuating quantities as a function of the starting point r_o for the B12/0.28rad/s case; (a) $\mathcal{R}_{ur}$, (b) $\mathcal{R}_{u\theta}$. The arrows indicate a decreasing r_o position, from the larger radii to the smaller.

the integral length scales defined as

$$l_{u\theta} = \int_0^{2\pi} \mathcal{R}_{u\theta}(r)\, r \mathrm{d}\theta, \tag{4}$$

at different radial locations and likewise for l_{ur}. The $\mathcal{R}_{ur}$ and $\mathcal{R}_{u\theta}$ as a function of radii are presented in figure 8 (a) and (b) respectively. Notwithstanding the turbulence intensity increasing with r (see § 3.4), Figure 8 suggests an increasing l with r, which further indicates that eddies are larger in size, on average, at larger r. In order to obtain an overall estimation of the longitudinal integral length scale in the FOV, TPC functions starting at different r_o are averaged, i.e. TPC lines shown in Figure 8 (b) are averaged, to give a single-valued global $\langle l_{u\theta} \rangle$ value for each case through integration. With this global length scale, the global Ro_G and Re_G can be estimated. The results are shown in table 2. The global quantities are listed in order to provide an overall view of the physical quantities in the camera FOV. They are defined by the spatial mean of the local quantities. For instance $\mathrm{Ro}_G = \langle |u| \rangle / (\Omega \langle l_{u\theta} \rangle)$ and $\mathrm{Re}_G = \langle |u| \rangle \langle l_{u\theta} \rangle / \nu$, where $\langle |u| \rangle$ is the spatial mean $|u|$ and $\langle l_{u\theta} \rangle$ is the spatial mean $l_{u\theta}$ defined by (4).

In table 2, Ro_G for each case is calculated using the single-valued impeller rotation rate Ω. This is done because, in this way, the flow is tantamount to

one in a rotational frame of reference spinning at a rate Ω; see (1) which is exclusively used to define Ro in all the previous turntable experiments.

Although the Ro_G listed here are slightly larger than $\mathcal{O}(1)$, which is viewed as a limiting condition in the previous studies and the linear theory mentioned in § 1, the value of Ro_G really depends on the way it is defined, particularly on the length scale used. In most previous works [11], the definitions of *macro*-Ro used is: $\mathrm{Ro}_M = (|u|/2)/(2\Omega M)$, where M is the characteristic size of the mesh used to generate turbulence. If we adopt this definition of Ro_M, and replace M by $\langle l_{u\theta} \rangle$, then the values of Ro_G in table 2 will be quartered. Note that the velocity scale in Ro_M is defined as $|u|/2$. Together with the factor 2 in the denominator, this gives an overall factor of 1/4.

3.4. The turbulence quantities

Since this type of flow is also a member of the turbulent flow family, it is also worth having a look at the turbulence quantities, i.e. the Reynolds stresses and the turbulence production. From the results of this section, we will also see a potential link between the estimated turbulence dissipation and the skewness $Sk\left(\omega_{\parallel}\right)$ in § 3.5.

Components of Reynolds stresses τ computed by 2DPIV are presented in Figure 9 in cylindrical coordinates. They are first calculated in Cartesian coordinates and then mapped onto cylindrical coordinates using simple trigonometry. One can easily notice that the number of baffles has a clear effect on the stress distributions. As the number of baffles is reduced, the peak of the stresses moves towards larger radii which is consistent with the trend in Figure 4. This is especially clear in the shear stress component. The radial and azimuthal components are of similar magnitudes and sum to the $|u|$ used in the calculation of Ro_G and Re_G. The strength of the Reynolds shear stress is relatively low, approximately one order of magnitude smaller.

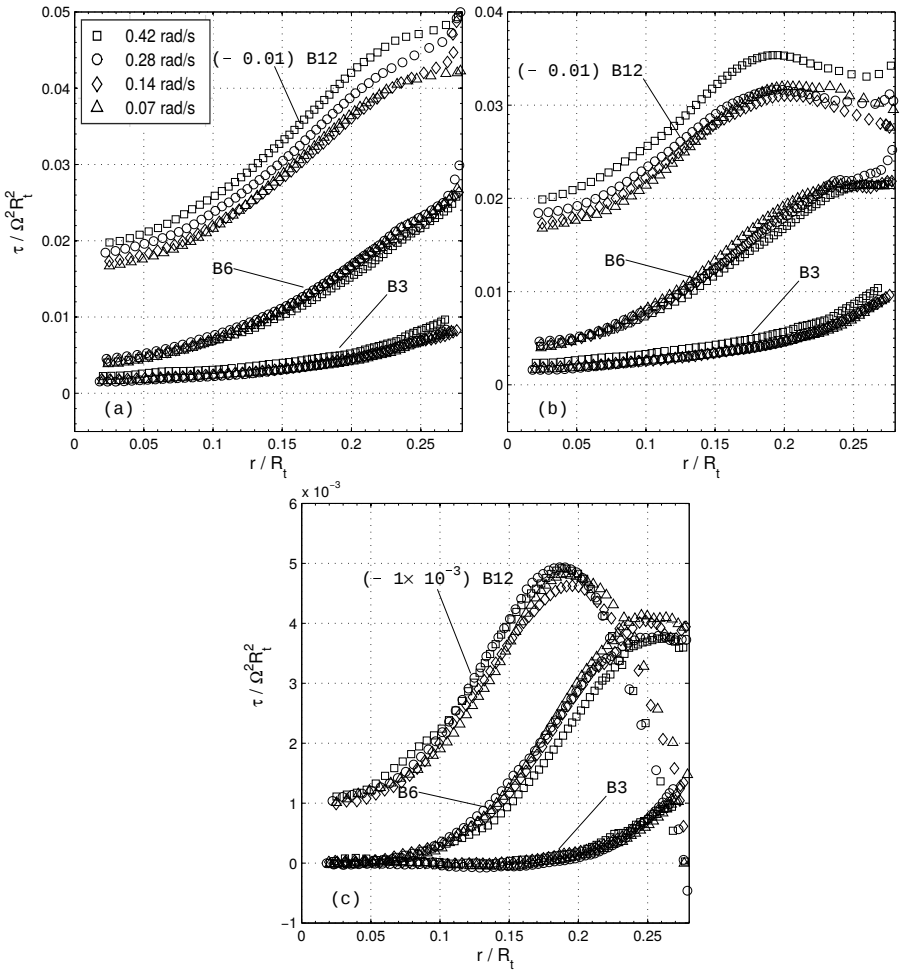

Figure 9: Reynolds normal and shear stresses τ as functions of radial distance r. (a): $\langle u_r' u_r' \rangle / \Omega^2 R_t^2$; (b): $\langle u_\theta' u_\theta' \rangle / \Omega^2 R_t^2$; (c): $\langle u_r' u_\theta' \rangle / \Omega^2 R_t^2$. B12 case is shifted upwards.

In cylindrical coordinates, turbulence production is written as

$$\begin{aligned}\mathcal{P}_{cyl} &= -\langle u_r' u_r' \rangle \frac{\partial U_r}{\partial r} - \langle u_\theta' u_\theta' \rangle \left(\frac{1}{r}\frac{\partial U_\theta}{\partial \theta} + \frac{U_r}{r} \right) \\ &\quad - \langle u_r' u_\theta' \rangle \left(\frac{\partial U_\theta}{\partial r} + \frac{1}{r}\frac{\partial U_r}{\partial \theta} - \frac{U_\theta}{r} \right) \\ &\quad - \langle u_z' u_z' \rangle \frac{\partial U_z}{\partial z} - \langle u_r' u_z' \rangle \left(\frac{\partial U_r}{\partial z} + \frac{\partial U_z}{\partial r} \right) \\ &\quad - \langle u_\theta' u_z' \rangle \left(\frac{\partial U_\theta}{\partial z} + \frac{1}{r}\frac{\partial U_z}{\partial \theta} \right), \end{aligned} \tag{5}$$

where only the first three terms are computable from 2DPIV data. The summation of the first three terms in (5) yields the 2D turbulence production. The resultant $\mathcal{P}_{2D}$ is shown in Figure 10. The production calculated from Cartesian coordinates is also plotted for the purpose of comparison for the B12/0.42rad/s case, which also serves as an evidence for the fact that the way of mapping components to cylindrical coordinates is fairly accurate. The contribution of the shear stress term $-\langle u_r' u_\theta' \rangle \left(\frac{\partial U_\theta}{\partial r} + \frac{1}{r}\frac{\partial U_r}{\partial \theta} - \frac{U_\theta}{r} \right)$ is found to be negligible, being one order of magnitude smaller than the two normal stress terms. Among the last three inaccessible terms, the magnitude of the last two is expected to be small because of weaker shear stresses $\langle u_r' u_z' \rangle$ and $\langle u_\theta' u_z' \rangle$ compared to normal stresses in general, which can be inferred from figure 9. For the last term $-\langle u_z' u_z' \rangle \frac{\partial U_z}{\partial z}$, $\frac{\partial U_z}{\partial z}$ can be computed from continuity $\frac{\partial U_z}{\partial z} = -\left(\frac{\partial U_r}{\partial r} + \frac{U_r}{r} \right)$. It is plausible that in rotating turbulence $\langle u_z' u_z' \rangle < \langle u_r' u_r' \rangle$ in terms of magnitude due to quasi-two-dimensionality. However, its exact value is not available from the current experimental arrangement.

The turbulence dissipation rate ϵ can be estimated from structure function $\left\langle [\Delta v]^2 \right\rangle$[2]:

$$\left\langle [\Delta v]^2 \right\rangle = \beta \epsilon^{2/3} r^{2/3}, \qquad \eta \ll r \ll l, \tag{6}$$

for r in the inertial subrange (between the Kolmogorov length scale η and the integral length scale l). The Kolmogorov constant β is a universal constant having a value of $\beta \sim 2$, for homogeneous turbulence only. Note that a recent study [1] found that $E(k_\perp) = 1.4\epsilon^{2/3} \left(\frac{l_\parallel}{l_\perp} \right)^{2/3} k_\perp^{-5/3}$ at modest Ro conditions, where $l_\parallel / l_\perp$ is a constant under steady condition. The exact value which β takes does

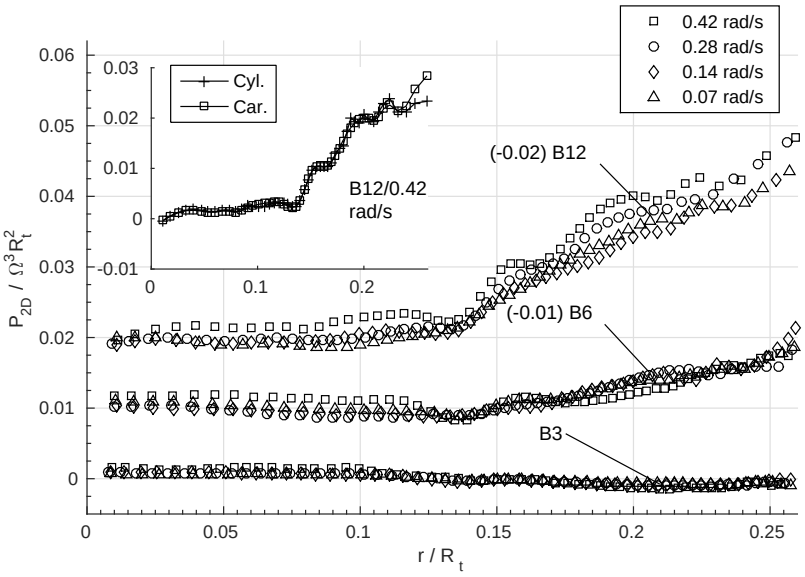

Figure 10: The resultant turbulence production $\mathcal{P}_{2D}$ computed by the available terms in (5). The inner plot compares the $\mathcal{P}_{2D}$ calculated from Cartesian and cylindrical coordinates.

not really matter since the main interest is the trend of the dissipation. Since the flow fields are not homogeneous in the r direction, the structure function has to be estimated in θ direction,

$$\left\langle \left[\Delta v\left(\theta\right)\right]^2 \right\rangle = \left\langle \left[u'_\theta\left(r,\theta+\theta_0\right) - u'_\theta\left(r,\theta_0\right)\right]^2 \right\rangle, \tag{7}$$

Therefore the argument r in equation 6 is along the azimuthal direction and actually takes the form $r\theta$ here. Figure 11 (a) shows an example of $\left\langle \left[\Delta v\left(\theta\right)\right]^2 \right\rangle$ versus $\left(r\theta\right)^{2/3}$ for the run case B12/0.28rad/s, at various radii. It can be seen that each line exhibits a linear part in the vicinity of $\left(r\theta\right)^{2/3} \approx 0.1$, and that the linear range shrinks as we approach the tank centre, following the arrow. The dissipation $\epsilon\left(r\right)$ can then be estimated using the slope of the linear part together with equation 6, and this is shown in figure 11 (b) for all the run cases. The B12 and B6 cases show a general increasing dissipation with radii r, while B3 cases display a substantial decreasing correlation range upto $r \sim 0.15R_t$.

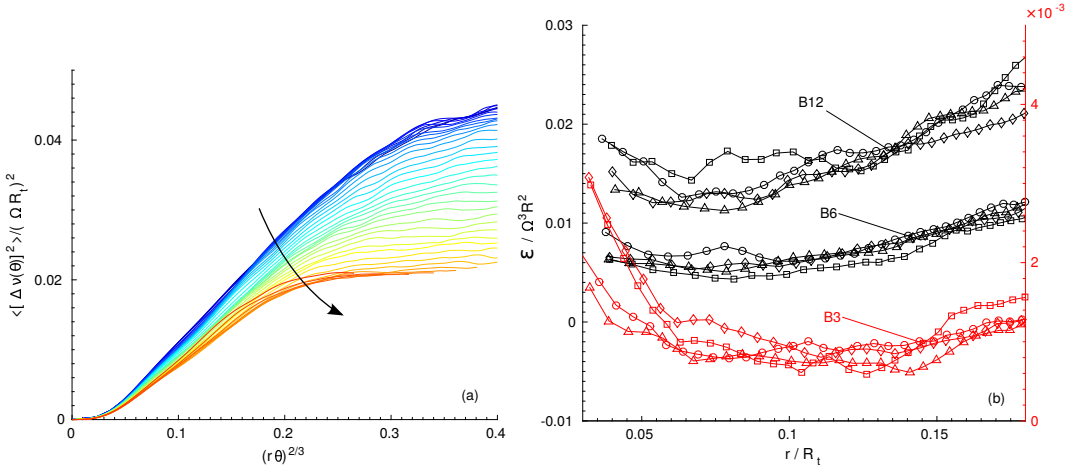

Figure 11: The estimated turbulence dissipation ϵ' from the longitudinal structure function $\left\langle [\Delta v\,(\theta)]^2 \right\rangle$. (a) structure function at decreasing radii for B12/0.28rad/s case, indicated by the arrow; (b) the estimated dissipation from equation 6; legends see Figure 10.

3.5. The effect of Ro on $Sk\left(\omega_{\|}\right)$

In this section, we investigate if there is a correlation between Ro and the local skewness of fluctuating vorticity $Sk\left(\omega_{\|}\right)$. The method used to calculate these two quantities is similar to the one used to compute the local azimuthal velocity as is shown in Figure 4. That is, an azimuthal averaging is applied for points having the same radii. The Ro based on the length scale $l_{u\theta}$ and $Sk\left(\omega_{\|}\right)$ are presented in Figure 12 as functions of r. One can also observe that at very large r in the B12 case, Ro seems to have reached maximum values and ceased climbing up and not surprisingly for the B6 and B3 cases, the increasing trend of Ro extends outside the FOV.

The shape of $Sk\left(\omega_{\|}\right)$ is generally noisier towards smaller r because firstly, skewness is a higher ordered quantity and secondly, there are less data points to average towards smaller radii, even though as shown in Figure 3, in each case statistical convergence is roughly achieved. The maximum $Sk\left(\omega_{\|}\right)$ is the physical quantity that one needs to pay particular attention to because it indicates the maximum extent of the dominance of cyclonic eddies over the anti-cyclonic

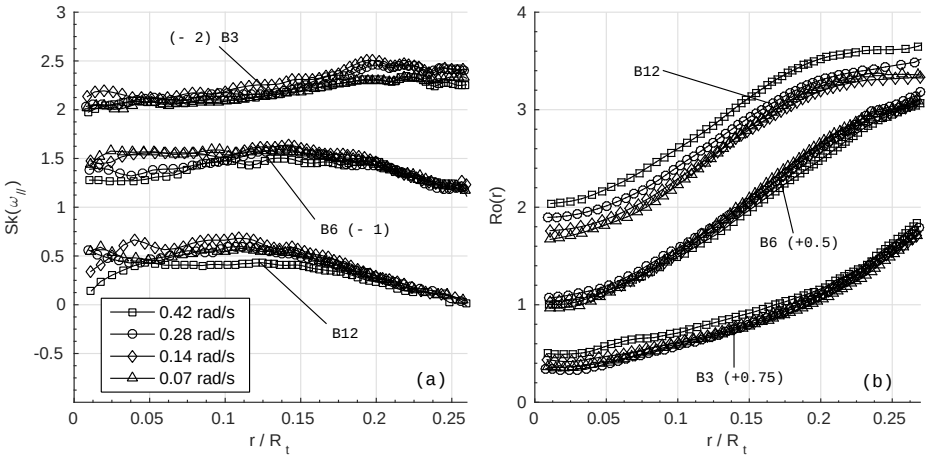

Figure 12: The local skewness of $\omega_{\parallel}$, $Sk\left(\omega_{\parallel}\right)$ (a) and the Rossby number as functions of radial distance r (b). B6 and B3 cases are shifted.

ones that can be detected in our FOV. It is reassuring to see that considering the mean trend (averaged over the 4 Ωs) for each baffle number case, the maximum $Sk\left(\omega_{\parallel}\right) \approx 0.5 \sim 0.7$ consistently. The location of the maximum value occurs from $r \sim 0.1R_t$ to $r \sim 0.2R_t$. Since the maximum $Sk\left(\omega_{\parallel}\right)$ is not locked geometrically by r, it then could be a function of $\mathrm{Ro}(r)$ instead. It turns out that if $Sk\left(\omega_{\parallel}\right)$ is plotted verses local Ro i.e. Figure 12 (a) is plotted against (b), a non-trivial outcome is obtained as shown in Figure 13 (a).

Figure 13 (a) suggests that the three groups of lines maximise themselves at around a universal $\mathrm{Ro}\langle l_{u\theta}, \Omega\rangle \approx 2$ and the maximum $Sk\left(\omega_{\parallel}\right)$ is about $0.5 \sim 0.7$. This is clearer if these lines are plotted together, which is shown by the line LPF0 in (b), where data points have a weakly skewed parabolic distribution with a single maximum value. As we depart from $\mathrm{Ro}\langle l_{u\theta}, \Omega\rangle \approx 2$, $Sk\left(\omega_{\parallel}\right)$ returns to less skewed values. The magnitude of the $Sk\left(\omega_{\parallel}\right)$ is a measure of the degree of symmetry breaking. The saturated skewness value is consistent with a previous finding [17] but is about half of another [11]. This is believed to be mainly due to the absolute PIV spatial resolution difference: the resolution in the latter [11] is significantly smaller than that in the former [17] and the current study. Another potentially important issue is that in this experiment, there is a strong

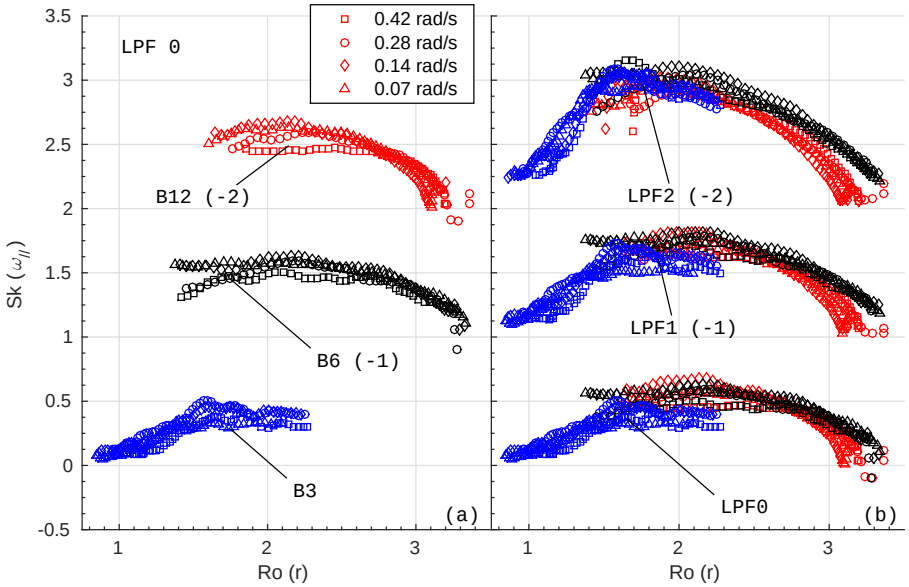

Figure 13: The local skewness, $Sk\left(\omega_{\|}\right)$ as a function of the local Rossby number. Abbreviation LPF: low pass filter. (a) The $Sk\left(\omega_{\|}\right)$ computed using the raw fluctuating vorticity $\omega_{\|}$, without applying LPF, with the cases B6 and B12 shifted upwards. (b) The effect of LPF kernel sizes. LPF0: kernel size 0, simply combines the data in (a) without any filtering; LPF1: kernel size $\sim 1 \times \langle l_{\omega} \rangle$; LPF2: kernel size $\sim 2 \times \langle l_{\omega} \rangle$. $\langle l_{\omega} \rangle$ is the spatial averaged length scale based on TPC of $\omega_{\|}$ field. LPF1 and LPF2 are shifted upwards.

relative motion between the bulk flow and the tank wall and baffles, where turbulence is generated. Close to the boundaries, the eddies that are shed tend to be anti-cyclonic. When these eddies penetrate through the bulk flow and reach the FOV, the ones that are still alive will tend to reduce the degree of symmetry breaking, i.e. the predominance of cyclonic eddies is likely to be diminished. This means that $\omega_{\parallel}$ in our experiment ought to be intrinsically less skewed than that in previous experiments, although this effect should be fairly small since the FOV is relatively far away from the tank boundary. A further discussion discussion on this is provided in § 4. It is worth emphasising again that $Sk\left(\omega_{\parallel}\right)$ here is calculated by considering all the eddies including those transient background turbulent eddies.

In order to isolate the effect of the larger organised eddies from these background eddies, the 2D $\omega_{\parallel}$ field is convolved by a low pass filter with a uniform kernel, similar to a previous study [12] for a Gaussian kernel. Two kernel sizes are applied which correspond to $1\times$ and $2\times$ the spatial mean eddy size $\langle l_{\omega}\rangle$ for each case. The characteristic eddy size l_{ω} is calculated from TPC of fluctuating vorticity field $\omega_{\parallel}$, similarly to equation 3 and 4 [17, 12]. From a mathematical standpoint, performing a uniform window low-pass filter smooths the data field without putting any weight in the central area; kinematically, when applied to $\omega_{\parallel}$, this locally integrated result corresponds to the *local fluctuating circulation* Γ in the measurement plane. It is then rational and particularly useful to remove the smaller background eddies and to highlight the ones which are equal and larger than the kernel size. The LPF is not applied to the $\mathbf{u}'$ field, hence Ro remains unchanged, since the local integration of velocity does not have a useful physical meaning. The effect of filtering is very clear in Figure 13 (b), where the maximum $Sk\left(\omega_{\parallel}\right)$ is more distinct due to higher values and the corresponding $\mathrm{Ro}\langle l_{u\theta}\Omega\rangle$ is slightly reduced to around 1.5. Furthermore, the curves are smoother, which suggests that the 'noise' in LPF0 mainly originates from high frequency background eddies.

It is worth noting that the shape of the estimated dissipation ϵ' shown in Figure 11 shares some similarities to the (upside-down) unfiltered skewness dis-

tribution in Figure 12 (a). The general trend of $Sk\left(\omega_{\parallel}\right)$ is in line with the ϵ' and the peak values happen at a similar r range for each baffle case. A possible link can be established between these observations based on earlier rotating turbulence experiments [11]. There is evidence showing turbulence dissipation rate in such a flow at Ro$\sim \mathcal{O}(1)$ is significantly suppressed than it is in homogeneous turbulence, for example in a flow generated by a grid mesh. This suggests that when $\omega_{\parallel}$ symmetry starts to break, the dissipation is inhibited. Therefore the distribution of $Sk\left(\omega_{\parallel}\right)$ has a physical link to the distribution of the turbulence dissipation rate as shown by the trends between the two quantities.

4. Discussion and Conclusion

This paper presents a 2DPIV experimental study of a special type of rotating flow. The flow is generated by the co-rotation of two impellers installed near the top and the bottom of a large quasi-cylindrical tank. Such flows are often found in common engineering applications, e.g. in pumps and mixing/stirring chambers. Due to the relative motion between the impellers and the tank wall, and the presence of purposely installed baffles, the flow in the central region of the tank has a relatively large turbulent Re but small Ro. Moreover, the mean flow in that region is found to be close to, but not exactly identical to the canonical solid-body rotation, which has been studied in detail before. Although the local rotational flow near the rotation axis is not solid-body, it is found to be Rayleigh stable and consequently some physical phenomena which are commonly noticed in previous low Ro solid-body rotating turbulence experiments are also found to occur in this experiment. This suggests that theories proposed for idealised solid-body rotating turbulence extend to the more realistic rotating flow presented here, although the proof of this validity is not the focus of this study.

The unique experimental configuration also allowed us to access various physical quantities from a different perspective. The experiment facility is the largest of its kind compared to all the earlier experiments (implying that bound-

ary effects are reduced as much as possible) but unlike those experiments the observer (the camera) is in a fixed frame of reference. Crucially, it is possible to control the turbulence level in the flow by means of a number of axisymmetrically attached turbulence generators: the Λ-shaped vortex shedding devices. This allows us to maintain the amount of turbulence at various statistically constant levels throughout our investigation.

From the turbulence quantity distributions, i.e. the Reynolds stresses, the turbulence production and the estimated dissipation, it is evident that these quantities are not homogeneously distributed. Turbulence intensity is higher towards outer radii near the tank wall. From structure functions, it is found that the shape of the estimated dissipation is in line with the distribution of $Sk\left(\omega_{\parallel}\right)$, notwithstanding a sensitive error depending on the linear fit range in figure 11 (a). This might be an evidence of the effect of the $\omega_{\parallel}$ symmetry breaking on the suppression of turbulence dissipation rate that has been commonly observed in previous studies [11, for example].

One may argue that the axially installed long Λ-shaped baffles may favour elongated columnar structures aligning along the rotation axis. Even if this is the case, the baffles should generally tend to favour the anti-cyclonic columns since the vortices shed by them rotate in the direction opposite to the bulk rotation. However, as is shown by the skewness (Figure 12 and 13), cyclonic eddies still dominate the anti-cyclonic ones; especially for large sizes, the effect of the cyclones seems to be overwhelming; see the low-pass filtered $\omega_{\parallel}$ in Figure 13. A more direct evidence for this can be obtained from the eddy size distribution over the FOV, which is the subject of future work.

The time t_d taken by turbulent eddies generated at the wall/baffle to diffuse to the FOV roughly scales as $\sqrt{\nu_t t_d} \sim (3/4)\, R_t$, the non-linear eddy turn-over time is $t_{nl} \sim l/u$, where l and u are the characteristic eddy length and velocity scales. A rough estimation of the ratio of these times scales indicates $t_d/t_{nl} \sim \left(R_t/l\right)^2 \left[u/\left(\Omega l\right)\right] = \left(R_t/l\right)^2$ Ro. A reasonable choice of the integral length scale l shows that any organised eddy diffusing from the wall to the FOV will most likely be killed by turbulence since $R_t \gg l$. Nevertheless in the FOV, some

organised eddies do survive at least one order of magnitude longer than t_{nl}. We will show, in a separate work, that the typical angular displacement of a turbulent eddy is $\phi_{nl} \sim \Omega t_{nl} \sim 1/\mathrm{Ro}$ and is typically 0.01 to 0.02 of a completed impeller revolution, which is well below one order of magnitude of some long-lived eddies. Therefore, these long-lived eddies are very unlikely to be associated with any boundary generated eddies.

Although our FOV is limited in size, it is sufficient for our study, since firstly, a much larger FOV would reach the radii where the flow tends to be Rayleigh unstable (due to the stationary tank wall, there is always an unstable region at larger radii) and boundary layer effects tend to be important; secondly, the $Sk\left(\omega_{\parallel}\right)$ maxima is observable within the FOV when all the cases are combined and plotted against local Ro in Figure 13. $Sk\left(\omega_{\parallel}\right)$ is an indication of the degree of symmetry breaking. This fact becomes even more apparent after small disorganised background turbulent eddies are filtered. The low-pass filtered result physically means that these flows have a stronger skewness towards cyclonic fluctuating local circulation around an area comparable to l_{ω} in the FOV. The critical Ro at which the strongest skewness occurs is found to be ~ 1.5 based on $l_{u\theta}$, while in terms of macro-Ro it is ~ 0.38 respectively. The fact that $Sk\left(\omega_{\parallel}\right)$ does not grow monotonically with decreasing Ro but reaches a peak at some intermediate Ro and then drops again at lower Ro agrees with the findings in solid-body rotating turbulence [5, 12]. Note also that this critical Ro is not a function of the baffle number, nor is it a function of radial distances from the rotation axis, i.e. it is independent of the turbulence condition at the tank boundary.

5. Acknowledgement

The authors would like to thank Professor P. A. Davidson for valuable discussions about the theoretical background of the current work.

References

[1] Bin-Baqui, Y. & Davidson, P. A. 2015 A phenomenological theory of rotating turbulence. *Phys. Fluids* **27**, 025107

[2] Davidson, P. A. 2004 Turbulence. *Oxford University Press* New York

[3] Davidson, P. A., Staplehurst, P. J. & Dalziel, S. B. 2006 On the evolution of eddies in a rapidly rotating system. *J. Fluid Mech.* **557**, 135–144

[4] Davidson, P. A., Kaneda, Y. & Sreenivasan, K. 2013 Ten chapters in turbulence *Cambridge University Press* Cambridge

[5] Deusebio, E., Boffetta, G., Lindborg, E. & Musacchio, S. 2014 Dimensional transition in rotating turbulence. *Phy. Rev. E* **90**, 203005

[6] Gallet, B.,Campagne, A., Cortet, P.-P. & Moisy, F. 2014 Cyclone-anticyclone asymmetry and alignment statistics in homogeneous rotating turbulence *Phys. Fluids* **26**, 035108

[7] Hopfinger, E. J., Browand, F. K. & Gagne, Y. 1982 Turbulence and waves in a rotating tank. *J. Fluid Mech.* **125**, 505–534

[8] Jeffery, G. B. 1922 The motion of ellipsoidal particles immersed in a viscous fluid. *Proc. R. Soc. Lond. A* **102**, 161–179

[9] Johnson, J. A. 1963 The stability of shearing motion in a rotating fluid. *J. Fluid Mech.* **17**, 337–352

[10] Kolvin, I., Cohen, K., Vardi, Y., & Sharon, E. 2009 Energy transfer by inertial waves during the buidup of turbulence in a rotating system. *Phy. Rev. Lett.* **102**, 014503

[11] Morize, C., Moisy, F. & Rabaud, M. 2005 Decaying grid-generated turbulence in a rotating tank. *Phys. Fluids* **17**, 095105

[12] Moisy, F., Morize, C., Rabaud, M. & Sommeria, J. 2011 Decay laws, anisotropy and cyclone-anticyclone asymmetry in decaying rotating turbulence. *J. Fluid Mech.* **666**, 5–35

[13] Naso, A. 2015 Cyclone-anticyclone asymmetry and alignment statistics in homogeneous rotating turbulence *Phys. Fluids* **27**, 035108

[14] Pinton, J. F., Chillà, F. & Mordant, N. 1998 Intermittency in the closed flow between coaxial corotating disks. *Eur. J. Mech. B/Fluids* **17(4)**, 535–547

[15] Savas, O. 2008 On flow visualization using reflective flakes. *J. Fluid Mech.* **152**, 235–248

[16] Sreenivasan, B., & Davidson, P. A. 2008 On the formation of cyclones and anticyclones in a rotating fluid. *Phys. Fluids* **20**(8), 085104

[17] Staplehurst, P. J., Davidson, P. A. & Dalziel, S. B. 2008 Structure formation in homogeneous freely decaying rotating turbulence. *J. Fluid Mech.* **598**, 81–105

[18] Tennekes, H. & Lumley, J. L. 1972 A first course in turbulence *MIT Press* 17^{th} printing 1999

[19] Tritton, D. 1992 Stabilisation and destabilisation of turbulent shear flow in a rotating fluid. *J. Fluid Mech.* **241**, 503–523

[20] Waleffe, F. 1993 Inertial transfers in the helical decomposition. *Phys. Fluids A* **5**(3), 667–685

[21] Smith, L. M. & Waleffe, F. 1999 Transfer of energy to two-dimensional large scales in forced, rotating three-dimensional turbulence. *Phys. Fluids* **11**(6), 1608–1622